Available online at www.ijournalse.org

Emerging Science Journal

(ISSN: 2610-9182)

Vol. 7, No. 5, October, 2023

Modeling Plasmonics and Electronics in Semiconducting Graphene Nanostrips

Talia Tene [1], Marco Guevara [2], Gabriel Moreano [3], Edisson Calderón [3], Nataly Bonilla García [4], Cristian Vacacela Gomez [5*], Stefano Bellucci [5*]

[1] *Department of Chemistry, Universidad Técnica Particular de Loja, 110160 Loja, Ecuador.*

[2] *UNICARIBE Research Center, University of Calabria, I-87036 Rende, CS, Italy.*

[3] *Facultad de Ingenieria Mecánica, Escuela Superior Politécnica de Chimborazo (ESPOCH), Riobamba 060155, Ecuador.*

[4] *Facultad de Ciencias, Escuela Superior Politécnica de Chimborazo (ESPOCH), Riobamba 060155, Ecuador.*

[5] *INFN-Laboratori Nazionali di Frascati, Via E. Fermi 54, I-00044 Frascati, Italy.*

Abstract

In recent decades, both academia and industry have shown noteworthy interest in investigating the semiconducting properties of graphene. Nevertheless, the lack of a suitable bandgap in graphene has restricted its practical applications in the current semiconductor industry. To overcome this limitation, graphene micro/nano-strips have been actively explored. The focus of the present study centers on modeling the electronic and plasmonic characteristics of graphene strips with varying widths: 2.7, 100, 135 nm, and 4 m. This analysis is conducted at ultralow energies (0.3 eV, or ~73 THz). We employ conventional density functional computations to estimate the Fermi velocity of graphene, refining the results via the GW approximation. Utilizing the accurate Fermi velocity, we employ a semi-analytical model to explore the ground state and plasmon properties (frequency and dispersion) of these graphene strips. Notably, this approach effectively replicates the density of states observed in narrow experimental graphene nano-strips (2.7 nm) grown on Ge(001) and, similarly, reproduces the plasmon spectrum found in synthesized graphene microstrips (4 μm) on Si/SiO2. Interestingly, our study also offers insights into the potential application of this approach in comprehending the plasmon frequency and plasmon dispersion of graphene nano-strips (~135 nm) acquired through liquid-phase exfoliation. The outcomes of this investigation present compelling evidence that the properties of graphene-based strips can be customized to fulfill specific requirements and applications. These findings hold significant promise for advancing graphene-based technologies, bridging the gap between fundamental research and tangible applications.

Keywords:

Graphene Micro/Nano-Strips;
THz Plasmons;
Electronics;
Fermi Velocity;
Semi-Analytical Model.

Article History:

Received:	21	April	2023
Revised:	20	September	2023
Accepted:	23	September	2023
Published:	01	October	2023

1- Introduction

Plasmons, intriguing quasiparticles arising from the synchronized oscillations of electrons within metallic or semiconductor materials, hold a multifaceted realm of potential [1]. These plasmonic phenomena exhibit remarkable versatility in their activation, driven by various mechanisms including light absorption, electron beam excitation, or interactions with other particles [2]. The characteristics of plasmons, however, are intricately linked to a range of factors. These encompass the inherent properties of the metal and dielectric medium, the specific geometry and morphology of the propagation surface, and even external parameters such as the wavelength and intensity of excitation light, the

* **CONTACT**: cristianisaac.vacacelagomez@fis.unical.it; bellucci@lnf.infn.it

DOI: http://dx.doi.org/10.28991/ESJ-2023-07-05-01

composition and thickness of the metal film, and the surface roughness. These variables collectively influence the resonant frequency and spatial distribution of plasmons, making them a highly adaptable and tunable resource [3].

The significance of plasmons transcends the realm of fundamental research, finding practical applications in various domains, including biosensing and surface-enhanced spectroscopy [4]. Their unique ability to interact with electromagnetic fields and concentrate energy at nanoscale dimensions has enabled advancements in ultra-sensitive sensors for detecting molecules and nanoparticles. Additionally, they enhance the performance of analytical techniques, offering unprecedented opportunities for exploring the intricacies of molecules and materials at the nanoscale. Consequently, plasmons are emerging as pivotal elements in cutting-edge technologies with far-reaching implications in fields such as materials science, optics, and biotechnology.

In recent years, there has been a significant leap in the understanding of plasmonic materials, with the emergence of innovative alternatives paving the way for exciting possibilities [5]. One such groundbreaking material is graphene, a two-dimensional (2D) carbon-based lattice with a honeycomb structure [6]. The unique electronic properties of graphene make it an exceptionally promising platform for both studying and controlling plasmons at the nanoscale [7]. Notably, plasmons in graphene present a host of advantages that surpass those of traditional plasmonic nanoparticles such as gold and silver. These include exceptional tunability, minimal losses, remarkable confinement capabilities, and rapid propagation speeds [8].

These outstanding attributes of graphene plasmons open up a wide spectrum of potential applications. They find relevance in fields such as advanced photodetectors and solar cells, enabling improved efficiency and sensitivity. Additionally, ultra-compact optical modulators based on graphene promise revolutionary advancements in data transmission and processing. In the realm of biological sensing, graphene plasmons offer unprecedented precision and sensitivity, allowing for the detection of molecular interactions. Furthermore, their utility extends into terahertz (THz) imaging and spectroscopy, where they enable high-resolution imaging and detailed material analysis in this challenging spectral range [9].

On an intriguing alternative front, plasmons have also been observed and predicted in graphene nano-strips (GNSs), unveiling a captivating avenue of exploration [10]. These GNSs represent slender ribbons of graphene, characterized by widths spanning from a few nanometers to a few micrometers and lengths ranging from several micrometers to millimeters. What sets GNSs apart are their distinctive advantages over traditional graphene sheets, including a tunable bandgap, enhanced electronic transport properties, improved optical characteristics, and the ability to tailor functionalization [11]. Both experimental and theoretical investigations have unveiled that GNSs can indeed support plasmons endowed with unique properties compared to those found in larger (pristine) graphene sheets [12]. The frequency of these GNS plasmons exhibits a dependence on the strip width, offering a remarkable degree of tunability through adjustments in either the strip width or the carrier density [13].

One remarkable consequence of plasmon confinement within GNSs is the substantial enhancement of the plasmonic field and a noteworthy reduction in plasmon damping, which, in turn, results in extended plasmon propagation lengths [14]. These attributes open up new panoramas in the realm of nanophotonics and plasmonics, enabling the design of ultra-compact and high-performance devices for an array of applications spanning from ultra-sensitive sensors to advanced optoelectronic devices. GNS-based plasmonics hold the promise of revolutionizing our ability to manipulate and utilize light at the nanoscale, thereby underpinning the development of next-generation technologies with unprecedented precision and efficiency.

Importantly, Fei et al. [15] conducted pioneering research that sheds light on the nuanced world of plasmonics within GNS arrays (Figure 2), uncovering not one but two distinct plasmon types [15]. The first of these plasmon species, known as the edge plasmon, exhibits a striking sensitivity to the strip width and shape. The resonance frequency of these edge plasmons can be finely tuned through modifications in the strip width, offering a remarkable level of control over their behavior and interactions [16]. In contrast, surface plasmons represent a different facet of GNS plasmonics. These plasmonic modes extend across the entire length of GNSs, propagating throughout the nanostrip. Unlike their edge counterparts, surface plasmons exhibit a more uniform and extended behavior, contributing to the unique plasmonic landscape within GNSs. Understanding and harnessing these surface plasmons is essential for exploiting the full potential of GNSs in the development of cutting-edge nanophotonic and plasmonic devices.

From a theoretical standpoint, investigating the properties of GNSs presents an exciting challenge that demands a diverse array of modeling techniques [17, 18]. While established methods such as density functional theory (DFT), tight-binding, and Green's function have proven invaluable, there are also dynamic and more computationally efficient alternatives, such as semi-analytical approaches [19].

For instance, when delving into the complexities of large GNSs, which encompass a substantial number of atoms, relying solely on numerical methods can become prohibitively computationally expensive. In such scenarios, semi-analytical approaches emerge as invaluable tools, offering a practical middle ground between purely atomistic (*ab initio*) strategies and numerical simulations. These semi-analytical methods leverage a combination of mathematical approximations and analytical solutions, allowing the exploration of the behavior and characteristics of GNSs efficiently.

This strategic shift in modeling not only accelerates the pace of research but also broadens the scope of inquiries into GNS properties, enabling investigations that might have been otherwise impractical. The availability of such versatile modeling approaches amplifies the ability to uncover the intricate details of GNS plasmonics and facilitates the design of tailored GNS-based devices for diverse applications in nanophotonics, materials science, and beyond.

Keeping this objective at the forefront, we have adopted a semi-analytical strategy [20] to comprehensively explore the electronic and plasmonic characteristics inherent to GNSs. This modeling strategy centers on the crucial determination of the effective electron mass, achieved through precise calculations of the charge-carrier velocity, specifically the Fermi velocity, in freestanding graphene using GW calculations. This key parameter is seamlessly integrated into the semi-analytical framework, facilitating a holistic examination of GNS properties. To further emphasize, the modeling approach begins by estimating the charge-carrier velocity parameter in the proximity of the Fermi energy and the Dirac point, where graphene electronic bands exhibit linear dispersions. This foundational step enables us to embark on a detailed investigation of the band structure and density of states (DOS) within GNSs.

Subsequently, we endeavor further into the realm of GNS plasmonics, focusing on the dispersion of plasmon frequencies and their tunability. This aspect is fundamental, allowing us to elucidate how GNS plasmon behavior can be finely controlled and tailored to serve specific applications. It is important to note that this versatile modeling approach extends beyond pristine GNSs. We have successfully adapted this strategy to scrutinize the properties of exfoliated (experimental) GNSs, broadening the scope of our research and facilitating a more comprehensive understanding of GNS behaviors in diverse forms and configurations. By employing this refined semi-analytical approach, we aim to make significant contributions to the expanding body of knowledge concerning GNS electronics and plasmonics at very low energies. In doing so, we hope to advance the frontiers of nanophotonics, materials science, and related fields where GNS-based technologies hold immense potential.

The following paper is organized as follows: Section 2 provides a brief overview of our modeling approach, which utilizes DFT computations and the GW approximation, along with the introduction of a tailored semi-analytical model for honeycomb-like micro/nano strips. In Section 3, we delve into a comprehensive analysis of ground-state calculations and plasmon properties specifically for graphene micro/nano-strips. Our study culminates in Section 4, where we synthesize the key insights and present our concluding remarks.

2- Theoretical Framework

To point out, the distinction between armchair-edge and zigzag-edge graphene nanoribbons, particularly those with widths below 10 nm, significantly impacts their characteristics. In contrast, GNSs with widths exceeding 100 nm, are less influenced by edge configurations. As an example, experimental data by Yang & Murali [21] has shown that edges have a significant effect on the transport characteristics of graphene when the strip width is 57 nm or less.

On the other hand, it is important to highlight that our current study builds upon our previous findings. In our earlier reports, we estimated the plasmonic properties using conventional DFT calculations based on local density approximation (LDA), where the DFT-LDA charge-carrier velocity served as a key input parameter [20]. Additionally, we successfully employed the same approach to predict the properties of wider graphene nanostrips [22]. Moreover, we explored the potential of graphene nanostrips for molecular sensing applications [23]. In light of these accomplishments, the objective of our present work is not to reiterate the previously established results. Instead, we aim to demonstrate the agreement of the refined modeling approach (see Figure 1) based now on the GW approximation with selected experimental observations. By doing so, we aim to establish its potential as an initial step in the theoretical characterization of more complex or similar systems [24-26].

2-1- Modeling Approach: Step 1

For details see Tene et al. [20], we begin our analysis by conducting plane-wave DFT computations of freestanding graphene, utilizing the Kohn-Sham (KS) formalism. The electronic structure calculations were carried out using the local density approximation (LDA) [27], by employing norm-conserving pseudopotentials [28]. The energy cutoff was set to ~680 eV and periodic graphene planes were replicated along the z direction with a vacuum distance of 20 Å. Geometric optimization is not considered in this analysis because in our previous work [29] it was found that its effects are marginal in the band dispersion at very low energies. The lattice constant was fixed at 2.46 Å. To obtain the linear band structure of graphene around the Dirac point, the calculations are performed using a Γ-centered Monkhorst-Pack grid [30] of 540×540×1.

With the ground-state and electron density, the converged KS electronic structure is used as a starting point in the GW calculation [31]. Hence, we introduce the $e-e$ interaction and correlation effect by the many-body GW self-energy. The vertex corrections were neglected in both the self-energy and the polarizability. The contour deformation method [32] was used to integrate over frequency. As well-known, Green's function and dynamically screened interaction can be constructed using the DFT-KS electronic structure.

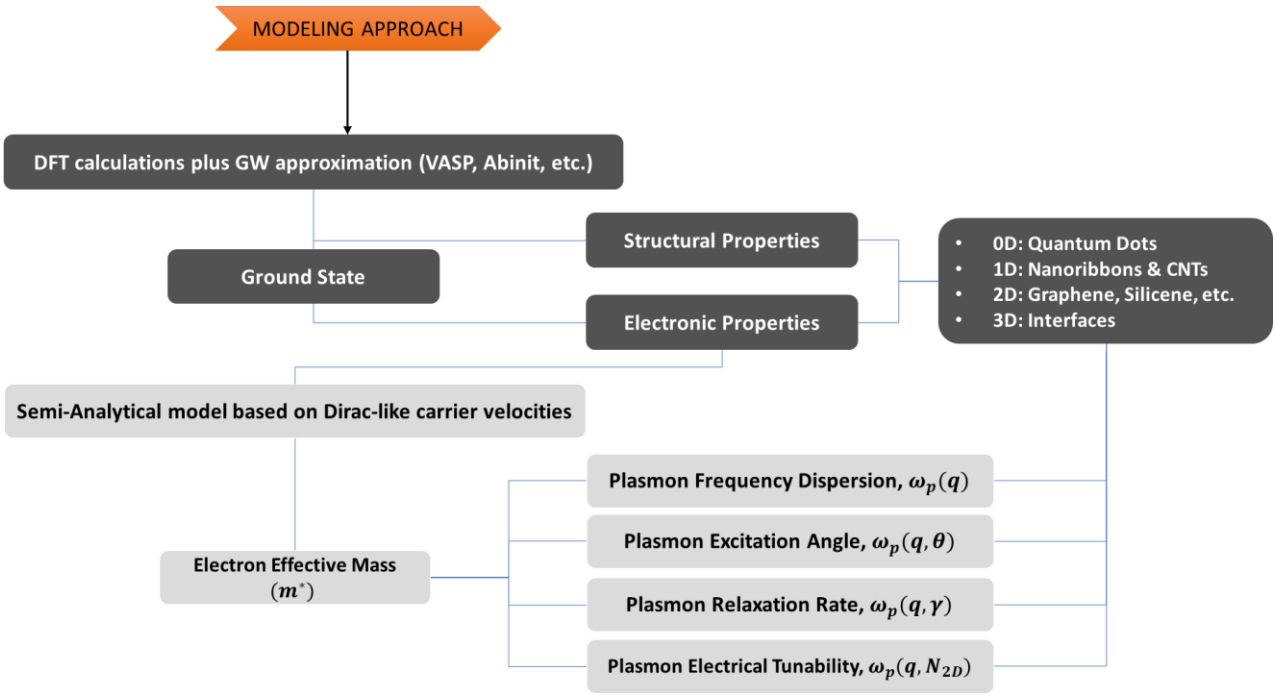

Figure 1. An overview flowchart illustrating the modeling approach in the present study

2-2- Modeling Approach: Step 2

For details see Tene et al. [19] and Popov et al. [19, 24]. In this section, our brief focus is on presenting and describing the main equations utilized for studying plasmonic properties. This equation serves as a fundamental tool from which subsequent analyses and investigations can be derived.

With this in mind, to scrutinize the plasmon properties of GNSs, we adopt the approach and system configuration (Figure 2) of Popov et al. [19], i.e., the plasmon frequency (ω_p) is expressed as:

$$\omega_p = \mathrm{Re}\left[\sqrt{\frac{2\pi e^2 N_{2D}}{\epsilon m^*} q\cos^2\theta - \frac{v^2}{4}} - i\frac{v}{2}\right] \quad (1)$$

where e is the electron charge, N_{2D} is the 2D charge density denoted also as $N_{2D} = N_{1D}/d$ (d is the vacuum distance between contiguous strips), ϵ is the dielectric constant, m^* is the effective electron mass, q is the momentum along the strip direction, θ is the plasmon excitation angle, v is the electron relaxation rate.

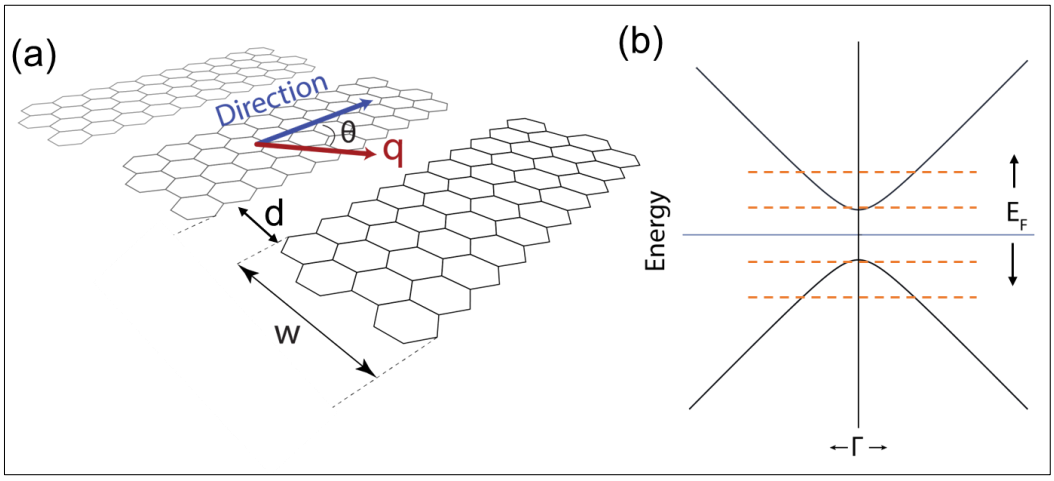

Figure 2. (a) Schematic representation of GNSs. (b) Hypothetical low-energy band structure of GNSs, showing the modulation of charge density by shifting the Fermi level to inject or eject charges

To calculate m^*, in Equation 1, the following expression is used by considering the charge-carrier velocity (v_F) of graphene from GW approximation:

$$m^* = \frac{\Delta}{2\,v_F^2} \quad (2)$$

where Δ is the bandgap of an isolated GNS, which can be estimated by considering the Planck constant ($\hbar$) and strip width (w), as follows:

$$\Delta = \frac{2\,\pi\,v_F\,\hbar}{w} \tag{3}$$

On the other hand, to compute the band structure of GNSs using the semi-analytical approach, it is essential to account for the quasi-one-dimensional confinement of charge carriers, which gives rise to multiple sub-bands (E_n) described as:

$$E_n = \pm\frac{\Delta}{2}\sqrt{n^2 + \frac{2p_{\parallel}^2}{m^*\Delta}} \tag{4}$$

Here n is the integer sub-band index and $p_{||}$ is the parallel wavevector.

3- Results and Discussions

3-1- The Charge-carrier Velocity of Pristine Graphene

To ensure equivalence with our previous report on silicene nano-strips [24], we present a comparable analysis in this work. By this idea, we aim to establish an additional comparison for readers between the findings of both studies (non-discussed here), while not the primary objective of our present study.

To start our discussion, Zhang et al. [33] initiated a comprehensive study focusing on the charge-carrier velocity of graphene. Their meticulous measurements resulted in a precise determination of the charge-carrier velocity, denoted as v_F, which was found to be equal to $v_F = 1.1 \times 10^6$ m s^{-1}. To further assess the accuracy of this experimental finding, it is essential to compare it with theoretical predictions. In Table 1, we present a comparative analysis by contrasting the experimental value with values obtained through two distinct computational methods: DFT-LDA and the GW approximation.

Table 1. The charge-carrier velocity of graphene. The estimated value by GW approximation is compared with the experimental result [33] and the predicted value by LDA-DFT [20]

Method	Value (10^6) (m s^{-1})	Variation percentage (%)
LDA-DFT	0.829	-24.64
GW	1.118	+1.64
Experimental	1.100	---

Firstly, the DFT-LDA calculations yielded a value of $v_F = 0.829 \times 10^6$ m s^{-1}. This outcome indicates an underestimation of the experimental value by approximately 24.64%. The deviation between the experimental data and the DFT-LDA prediction highlights certain limitations in the theoretical framework, emphasizing the need for a more accurate model. Hence, the GW calculations provided a different perspective. According to these calculations, the charge-carrier velocity was determined to be $v_F = 1.118 \times 10^6$ m s^{-1}. In this case, the GW approximation displayed only a marginal overestimation of the experimental result, with a deviation of merely 1.64%. This demonstrates that the GW method offers a notably improved agreement with the experimental findings compared to DFT-LDA.

This analysis underscores the importance of choosing appropriate computational methods to accurately model and understand the behavior of nanomaterials such as graphene. In particular, the differences in accuracy between DFT-LDA and the GW approximation in predicting the charge-carrier velocity of graphene stems from their treatment of strong electronic correlations, quasiparticle excitations, and energy gaps. Conventional DFT, often reliant on approximations and exchange-correlation functionals, may struggle to capture these critical aspects of graphene electronic structure accurately. In contrast, the GW method explicitly accounts for electron-electron interactions and quasiparticle excitations, providing a more reliable approximation that aligns better with experimental findings.

To provide evidence of the previous statement, Figure 3 compares the well-known band structure of graphene using two different calculation methods: DFT-LDA (solid black line) and quasi-particle GW (dashed red line). The conduction and valence bands show noticeable effects of exchange and correlation, but these effects do not critically modify the band shape. On the other hand, the Dirac cone also experiences a pronounced effect, increasing energy and linear dispersion around the K point, suggesting an increase in the charge-carrier velocity. However, as the energy increases, this effect gradually disappears, and the bands appear to be very similar, indicating that the conduction bands remain unchanged [24].

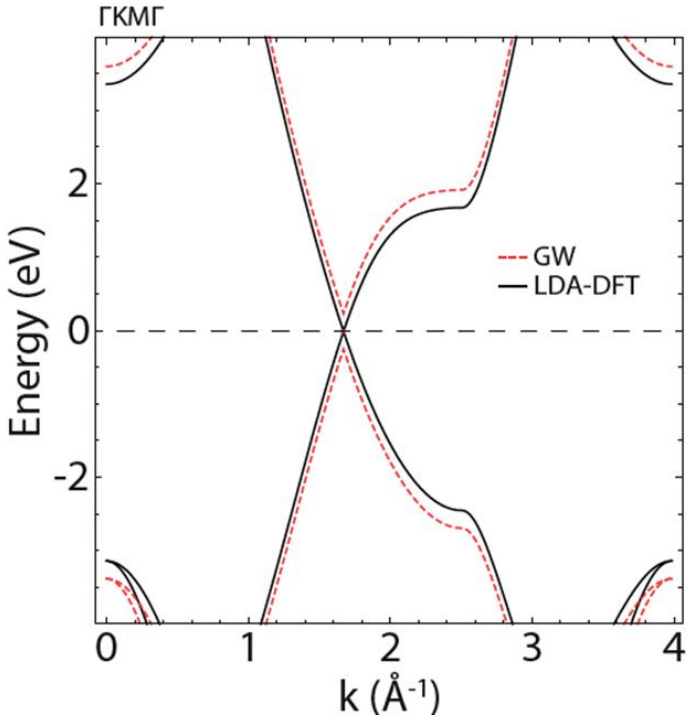

Figure 3. The band structure of graphene is computed by LDA-DFT (red) and GW (black) calculations

Keeping this in mind, let us now shift our focus to the Dirac point (K point) region, as shown in Figure 4-a. The black and green dots represent energy-momentum data obtained from the conduction (π^*) and valence (π) bands, respectively, using the GW calculations. By performing a linear fit (cyan line) on these data, we estimated the charge-carrier velocity (the same procedure for DFT-LDA calculations was applied, in Figure 5). Within the range of ± 0.04 Å^{-1} (setting the K point as zero) and ± 0.3 eV (setting the Fermi level as zero), we observed a clear linear dispersion of electron energy, which aligns with the expression of the Dirac cone approximation [19, 20], denoted as

$$E(\mathrm{k}) = \pm \hbar \mathrm{v_F} |\mathrm{k}| \tag{5}$$

where $E(\mathrm{k})$ is the energy of electrons (holes) at a certain wave vector (k) and $|\mathrm{k}|$ is the magnitude of the wave vector.

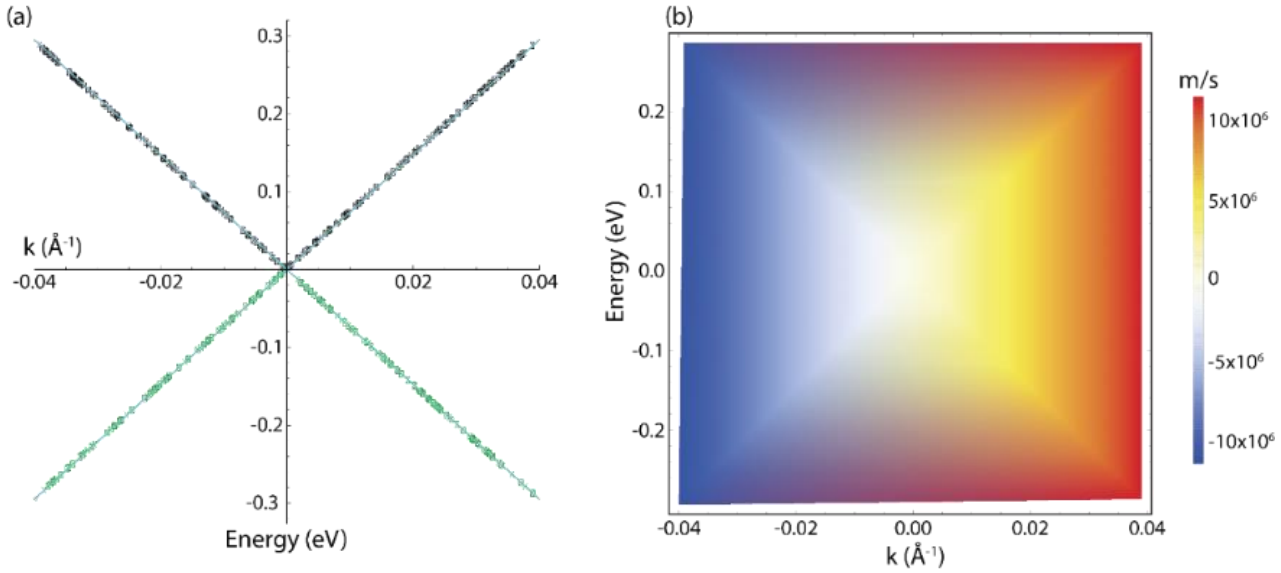

Figure 4. (a) GW Band structure of graphene at the K-point and around the Fermi level, featuring the π and π^* energy bands in green and black respectively. The cyan line indicates a linear fit. (b) A color plot depicting the charge-carrier velocity (10^6 m/s) of graphene in the vicinity of the K-point. The plot shows how the velocity changes with energy and wavevector. The negative value of charge-carrier velocity refers to the velocity in the valence band.

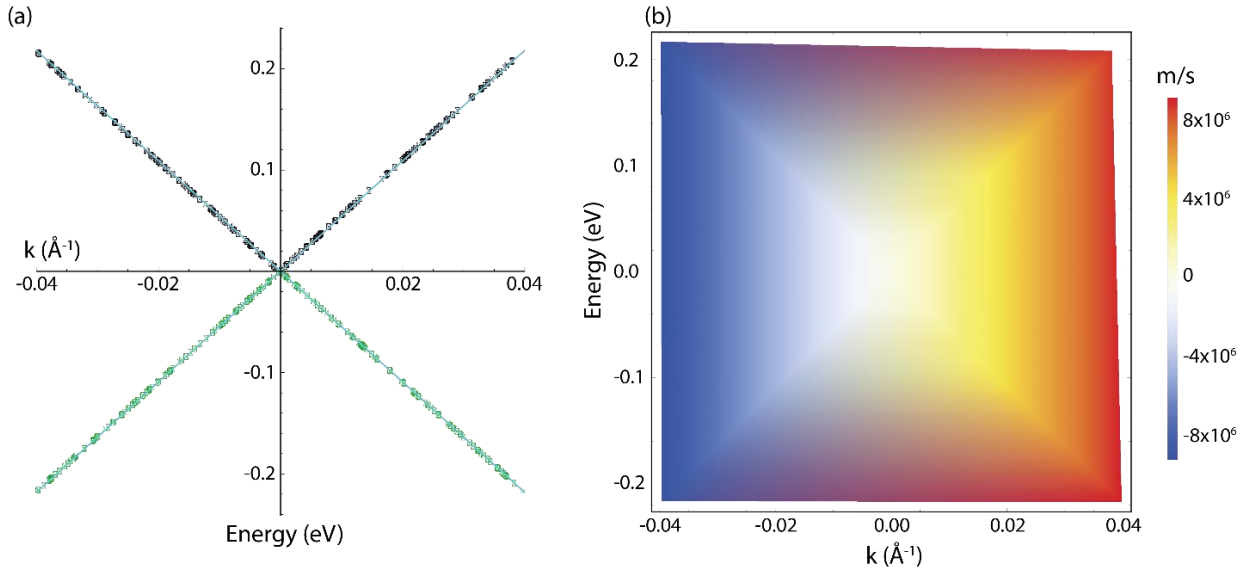

Figure 5. (a) DFT Band structure of graphene at the K-point and around the Fermi level, featuring the π and π^* energy bands in green and black respectively. The cyan line indicates a linear fit. (b) A color plot depicting the charge-carrier velocity (10^6 m/s) of graphene in the vicinity of the K-point. The plot shows how the velocity changes with energy and wavevector. The negative value of charge-carrier velocity refers to the velocity in the valence band.

In Figure 4-b, a noteworthy observation emerges: the charge-carrier velocity exhibits a pronounced linear correlation concerning both energy and wave vector. This linear behavior, however, is discernible within a specific energy window, approximately ± 0.25 eV. Beyond this range, the distinct lines representing this linear trend gradually diminish in intensity. These findings hold significant importance for our study, particularly in the context of the semi-analytical model we employ, which relies heavily on this linear relationship. The ability to pinpoint the extent of this linear regime aids in establishing the boundaries of the model and its applicability. In essence, we can assert that the semi-analytical model is valid within an energy span of roughly ± 0.25 eV, corresponding to a frequency limit of approximately 60 THz.

Remarkably, these observations are similar to our DFT-LDA calculations, which were exhaustively discussed in Tene et al. [20]. Consequently, the semi-analytical model can be confidently applied within an even narrower energy range of approximately ± 0.2 eV, corresponding to an approximate frequency limit of 50 THz, as illustrated in Figure 5-b.

3-2- Electronics Features of GNSs

Figure 6 provides an insightful exploration of the influence of strip width on the bandgap, a crucial property in GNSs. This impact is illustrated by the two distinct curves: the red line, representing the bandgap calculated using the GW approximation, and the blue line, which depicts the DFT-LDA approach. The data unveils a remarkable trend of exponential bandgap reduction, irrespective of whether the charge-carrier velocity is determined via the GW approximation or the DFT-LDA approach. What makes this observation particularly intriguing is how this reduction varies depending on the width of the GNS.

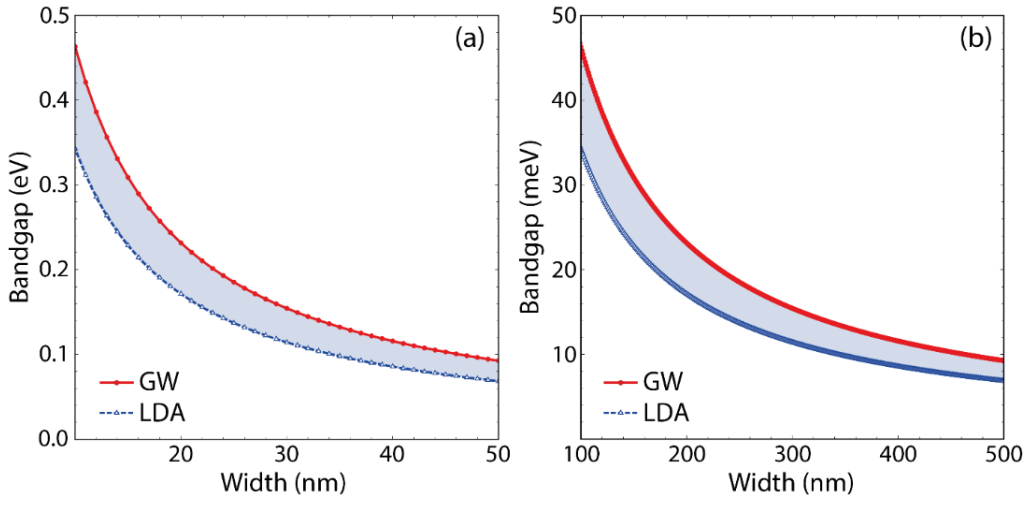

Figure 6. The Bandgap values of GNSs ranging (a) from 10 to 50 nm and (b) from 100 to 500 nm. For comparison purposes, the plots also include the variation of bandgap considering the charge-carrier velocity computed by GW calculation ($v_F = 1.118 \times 10^6$ m s^{-1}) and DFT-LDA ($v_F = 0.829 \times 10^6$ m s^{-1}).

For narrow GNSs, with widths spanning from 10 to 50 nm (Figure 6-a), a substantial transformation in the bandgap is evident. In this case, the bandgap undergoes a considerable decrease, transitioning from the eV scale to much lower values. Conversely, in wider GNSs, ranging from 100 to 500 nm (Figure 6-b), the bandgap exhibits a far more slight reduction, typically on the order of a meV.

It is noteworthy that the DFT-LDA calculations consistently yield lower bandgap values in comparison to the results derived from the GW approximation. On average, this difference amounts to approximately 23.8%. This intriguing contrast implies that bandgap predictions obtained through the DFT-LDA method should be approached with caution due to their propensity to underestimate the actual bandgap values. This insight underscores the importance of selecting appropriate computational methods, especially when dealing with the bandgap of GNSs.

Expanding upon our analysis of the numerical values obtained through the GW-charge-carrier velocity for graphene, Table 2 provides a comprehensive overview of key properties: bandgaps and effective electron masses, focusing on selected nano-strips. Notably, the obtained values highlight a compelling trend. For instance, the 100-nm-wide nano-strip showcases a bandgap value of approximately 46 meV. In stark contrast, the 500-nm-wide counterpart exhibits a notably reduced bandgap, measuring approximately 9 meV. This striking observation underscores the inverse relationship between strip width and bandgap. Specifically, as the width of the nano-strip increases by a factor of five, the bandgap consistently decreases in proportion. This trend is not limited to just bandgap values; it extends to the effective electron mass as well. When we compare identical systems with varying strip widths, we find that the effective electron mass also follows a similar pattern, demonstrating a proportional decrease as the nano-strip widens.

Table 2. Bandgap and effective electron mass of selected GNSs. m_0 is the electron rest mass

Width (nm)	Bandgap (meV)	$m^* \times m_0$ (10^{-3})
100	46.32	3.25
200	23.16	1.62
300	15.44	1.08
400	11.58	0.81
500	9.26	0.65

This systematic exploration of bandgap and effective electron mass variations across different nano-strip widths offers valuable insights into the behavior of graphene nanostructures, shedding light on how their electronic properties evolve with changing dimensions.

To further contextualize these findings, the decrease in bandgap and effective electron masses as the strip width increases can be explained by considering the quantum confinement effect and the evolving electronic structure as a function of strip width, as follows:

- Quantum Confinement Effect: GNSs are essentially narrow strips of graphene, and their electronic properties are strongly influenced by quantum confinement. In narrower strips, the lateral confinement is more significant, leading to quantization of energy levels. As the strip width increases, the quantum confinement effect becomes less pronounced.
- Edge States: GNSs have distinctive edge states that play a crucial role in their electronic properties. In narrower strips, the edge states are more localized and strongly affect the bandgap. These edge states introduce additional energy levels within the bandgap, effectively increasing it. As the strip width increases, these edge states become less confined, causing a reduction in their influence on the bandgap.
- Wavefunction Overlap: In narrow GNSs, the wavefunctions of electrons in the valence and conduction bands are more confined to the strip edges. This increased confinement results in a larger effective mass for charge carriers, contributing to a higher effective electron mass. As the strip width increases, the wavefunctions become less confined, leading to a decrease in effective electron masses.
- Delocalization of Electronic States: In wider GNSs, the electronic states become more delocalized across the strip width. This delocalization reduces the energy separation between the valence and conduction bands, resulting in a smaller bandgap. Additionally, the reduced localization of electronic states at the edges contributes to a decrease in effective electron masses.

Additionally, we point out that the obtained values of effective electron mass for the various nano-strips are consistent, in terms of orders of magnitude, with both experimental findings and predictions from more advanced models [34, 35].

To gain a deeper understanding of the electronic characteristics of GNSs with widths of 100 nm and 500 nm, we delve into a more detailed analysis by examining the band structure and density of states (DOS) within a ± 70 meV energy range, as illustrated in Figure 7. Upon closer inspection of these electronic properties, a couple of intriguing phenomena come to light:

- Firstly, when comparing the two systems, a distinctive quadratic energy dispersion of both the conduction and valence bands near the Γ point becomes evident. This quadratic dispersion pattern reflects the unique electronic behavior of GNSs in the vicinity of the Γ point, which resembles the behavior of pristine graphene.
- Additionally, the comparison between the 100 nm and 500 nm wide nano-strips reveals a noteworthy distinction. The 500 nm wide nano-strip exhibits a considerably greater number of energy bands within the same energy range, indicating a higher density of electronic states. This augmentation in the number of bands is a consequence of the broader lateral extent of the wider nano-strip, allowing for more quantum states to be accommodated.

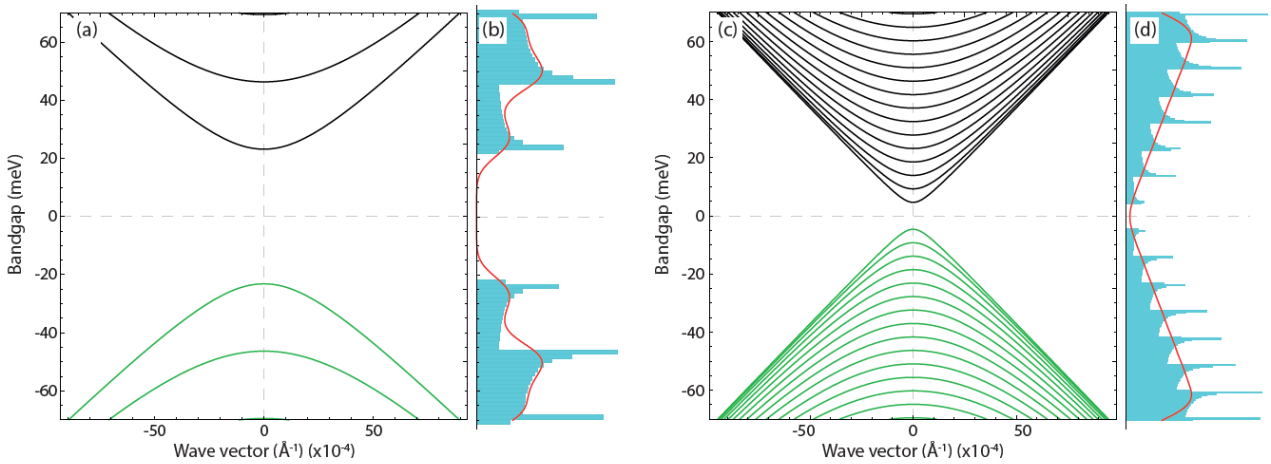

Figure 7. Band structure and density of states (DOS) of (a, b) 100 nm wide GNS and (c, d) 500 nm wide GNS. DOS is calculated from the energy-momentum data list by using a conventional histogram with equal bin widths. The red line is the smoothed curve of the histogram.

Furthermore, it is intriguing to observe that as the width of the nano-strips increases, the energy gaps between these bands decrease. In the case of a 500 nm width nano-strip, these bands tend to converge, approaching the same "energy state". This behavior bears a striking resemblance to the electronic structure of pristine graphene, as demonstrated in Figure 3, highlighting the transition from the confined electronic states in narrower nano-strips to a more continuous and graphene-like electronic structure as the nano-strips widen.

It is noteworthy that the DOS plots for nano-strips with widths of 100 nm (Figure 7-b) and 500 nm (Figure 7-d) exhibit multiple peaks, each corresponding to the bands observed in the band structure plots (Figures 7-a and 7-c, respectively). An important outcome is that applying smoothing to the DOS histogram (red line) can result in a narrower bandgap for these systems. For example, the 100 nm wide nano-strip demonstrates a bandgap of approximately 35 meV (compared to approximately 46 meV without smoothing, as shown in Table 2), while the 500 nm wide nano-strip exhibits a bandgap of about 7 meV (compared to approximately 9 meV without smoothing, as presented in Table 2)

It is important to note that we have used the same effective electron mass for all bands, with only the value of n (Equation 4), being changed. While the effective electron mass of each band, both conduction and valence bands, can be accurately calculated using *ab initio* methods, the challenge lies in the fact that systems as wide as those analyzed in this study are currently beyond the capabilities of available calculators worldwide based on atomistic approaches. This is where the semi-analytical model offers its advantages and provides interesting outcomes:

- For instance, Equation 3 gives realistic predictions for experimentally realized GNSs from 15 to 90 nm wide (Figure 8-a), and
- Even for more sophisticated methods when working with ultra-narrow GNSs ranging from 1.0 to 2.7 nm (Figure 8-b).

Our study takes a significant step forward by applying the semi-analytical model to unravel the electronic properties of an ultra-narrow 2.7 nm wide nano-strip. This specific nano-strip width was experimentally observed by Kiraly et al. on a Ge(001) substrate [38]. Our findings, presented in Figure 9-a, provide a critical insight: this nano-strip exhibits a substantial bandgap of approximately 1.7 eV. This observation is further substantiated by the DOS analysis displayed in Figure 9-b, which aligns coherently with our earlier analyses. The remarkable aspect of our investigation is the ability of the smoothed curve (depicted as the red line) in the DOS histogram to perfectly replicate the experimental results (illustrated as blue dots) obtained through scanning tunneling spectroscopy (STS) measurements, as showcased in Figure 9-c [38]. This level of agreement between theoretical predictions and experimental data is quite impressive, particularly considering the ultra-narrow width of the nano-strip. It is worth emphasizing that, as we have previously noted, the specific edge configurations (armchair or zigzag) of nano-strips play a pivotal role in determining their properties at such narrow widths. Despite this, the semi-analytical model, which is based on the charge-carrier velocity of freestanding graphene, not only closely matches the experimental DOS but also aligns well with the bandgap observed in the experimental data (≥ 0.9) [38].

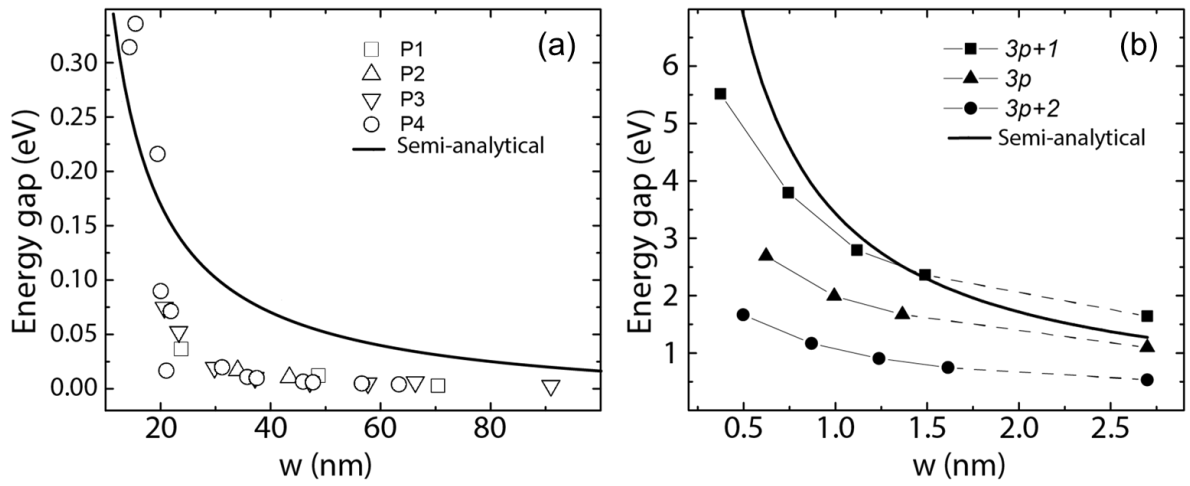

Figure 8. (a) Bandgap as a function of the ribbon width for experimentally realized graphene nanoribbons [36] compared to the GW-semi-analytical model (solid line). (b) Bandgap variation for narrow-wide graphene nanoribbons predicted by the GW approximation [37] compared to the GW-semi-analytical model (solid line).

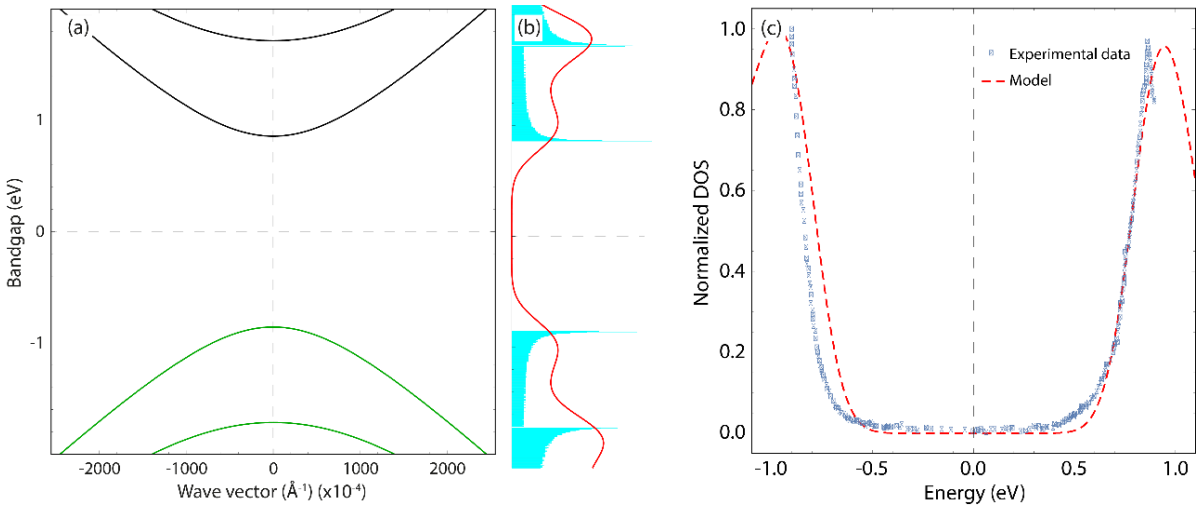

Figure 9. (a) Band structure and (b) DOS of 2.7 nm wide GNS. (c) Comparison of predicted DOS of 2.7 nm GNS (dashed red line) with the similar sample grown on Ge(001) (blue dots)

This intriguing convergence between theoretical predictions and experimental findings suggests that the graphene nano-strip on the Ge(001) substrate behaves remarkably as freestanding graphene in terms of its electronic properties. This evidence bolsters our confidence in the reliability and applicability of the semi-analytical model, paving the way for its use in the investigation of electronic and plasmonic properties in similar nanostructures such as silicene or germanene nano-strips.

3-3- Plasmonic Properties of Graphene Micro-strips

Before embarking on the comprehensive analysis of the plasmonic properties, it is crucial to establish a foundational understanding of the key parameters outlined in Equation (1). These parameters encompass essential factors such as the effective electron mass (m^*), charge density concentration (N_{2D}), plasmon excitation angle (θ), and electron relaxation rate (ν). Importantly, these parameters can be adjusted, sometimes without immediate physical context or insight. Recognizing this inherent flexibility, our primary objective in this study is to steer clear of arbitrary parameter manipulation. Instead, we place a strong emphasis on deriving these values through rigorous means, either by extracting them directly from experimental data or by leveraging predictions generated through advanced models.

By adopting this approach, we ensure that the values assigned to these parameters are grounded in empirical evidence or supported by robust theoretical frameworks. This not only enhances the credibility and reliability of our subsequent plasmonic property analyses but also aligns our research with a more principled and physics-driven methodology, providing a solid foundation for our investigations into the behavior and applications of plasmonic phenomena in GNSs.

Keeping this in perspective, let us delve into a practical application of the semi-analytical model. We utilize this model to replicate and understand experimental observations regarding THz plasmons in graphene micro-strips as

illustrated in Figure 10. Hence, to validate the accuracy of the modeling approach, we conduct a meticulous comparison, focusing on the maximum of the plasmon peak, against empirical data provided by Ju et al. [39]. The methodology employed for determining the theoretical plasmon peak position follows the approach detailed in our previous work [24]. Accordingly, the parameters used in Equation 1 are obtained from experimental measurements, i.e., $w = 4$ μm, $m^* = 0.8 \times 10^{-4} m_0$, $N_{2D} = 1.5 \times 10^{13}$ cm^{-2}, and $v = 8.71 \times 10^{13}$ s^{-1} (electron mobility of 1000 cm^2 V^{-1} s^{-1})

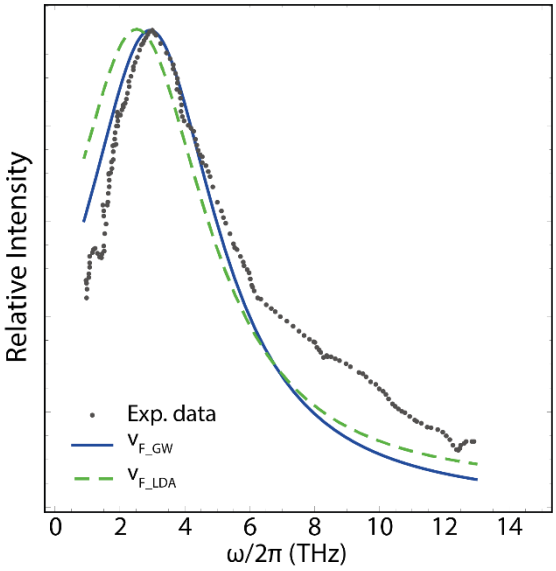

Figure 10. Comparison of the maximum of the plasmon peak (black line) at $q \approx 100$ cm^{-1} with experimental measurements (black dots), using parameters extracted from the same measurements

Notably, the semi-analytical model, coupled with the charge-carrier velocity determined via the GW approximation (blue line), achieves a remarkable feat: it precisely replicates the experimental spectrum of THz plasmons in graphene micro-strips. This agreement becomes especially apparent when we observe the maximum of the plasmon peak [24], confidently positioned at approximately 3 THz. It is important to note that when we employ the charge-carrier velocity obtained from DFT-LDA calculations, the model exhibits a discernible shift toward lower frequencies (green dashed line). This outcome serves as a compelling testament to the efficacy of the semi-analytical model in predicting the intricate behavior of THz plasmons in graphene micro-strips. Moreover, it underscores the critical significance of accurate parameter estimation for modeling studies. By ensuring that the model incorporates parameters derived directly from experimental measurements, we bolster its ability to faithfully capture real-world phenomena.

However, it is prudent to recognize that the precision and capacity to replicate experimental data, as demonstrated here, may be influenced by various factors. These factors can encompass the specifics of:

- The experimental setup
- The unique characteristics of the samples
- The inherent variability in experimental conditions.

Therefore, it remains essential to undertake further in-depth investigations and validation studies to gain a comprehensive understanding of THz plasmons in these systems.

3-4- Tunning the Plasmon Response in GNSs

Having established the ability of the semi-analytical model to faithfully replicate electronic behavior [38] and plasmonic phenomena [39], we now shift our attention to a compelling study: the tunability of plasmonic properties in nano-strips with widths exceeding 100 nm. This investigation holds significant importance, as it aligns with the pioneering work of Fei et al. [15], who successfully crafted nano-strips with widths comparable to those examined in the present work, ranging from 155 to 480 nm. Hence, our focus in studying the plasmon frequency dispersion lies in the parameter of charge density (N_{2D}). However, it is essential to highlight that, as demonstrated in our prior studies [20, 22-24], we possess the capability to explore the other critical parameters encompassed within Equation 1 with relative ease.

Furthermore, the choice of N_{2D} as the parameter of interest is notably strategic. This selection is rooted in the plasmon mode we investigate, which pertains to surface plasmons. These surface plasmons are known to propagate along the middle of the strip, following the longitudinal direction of the strip [40]. Given that the width of the strip extends to the order of tens of nm, we can effectively treat the strip as a quasi-2D system.

To further emphasize, studying plasmon properties as a function of 2D charge density is of paramount importance for several key reasons:

- Tailoring Plasmonic Devices: Plasmonic properties are highly sensitive to the charge density of the material. By systematically investigating how plasmons respond to changes in 2D charge density, we gain the ability to finely tune and tailor plasmonic devices for specific applications. This knowledge is crucial for optimizing the performance of plasmonic sensors, modulators, waveguides, and other nanophotonic components.
- Designing Efficient Plasmonic Sensors: Plasmonic sensors rely on the interaction between surface plasmons and analytes to detect minute changes in refractive index or molecular binding events. Understanding how the plasmon resonance frequency varies with charge density enables the design of sensors with enhanced sensitivity and specificity. This, in turn, improves the capabilities of biosensors, chemical sensors, and environmental monitoring devices.
- Optimizing Plasmonic Energy Conversion: Plasmonic materials are used in various energy conversion technologies, including photodetectors and solar cells. By studying the dependence of plasmonic properties on 2D charge density, these collective excitations can optimize the absorption and conversion of light into electrical energy.
- Enhancing Plasmon-Driven Nanophotonics: Plasmonics plays a vital role in nanophotonics, enabling the manipulation of light at the nanoscale. Understanding how charge density affects plasmonic resonances allows for the design of more efficient plasmonic waveguides, nanoantennas, and optical modulators. These advancements have direct implications for telecommunications, data processing, and integrated photonics.
- Addressing Environmental and Energy Challenges: Plasmonic materials are being explored for applications in environmental monitoring, energy harvesting, and catalysis. By studying how 2D charge density impacts plasmonic properties, one can develop more effective plasmonic catalysts for chemical reactions, leading to cleaner and more efficient energy conversion processes.

With this in mind, previous works have reported 1D charge densities (N_{1D}) in isolated GNSs on the order of $N_{1D} \approx 10^{15}$ cm^{-1} [40, 41], although the exact value can vary depending on aspects such as strip size, doping, or geometric factors. Indeed, according to the expression $N_{2D} = N_{1D}/d$ (see Section 2), the charge density decreases as the distance between adjacent nano-strips increases (see Table 3). For instance, if the vacuum distance between the nano-strips is increased from 10 nm to 100 nm, the charge density decreases by an order of magnitude. However, it is worth noting that in this scenario, the Fermi level (E_F) only decreases by almost three times. The values presented in Table 3 are precisely those utilized to examine the impact of charge density.

Table 3. Variation of charge density and Fermi level as a function of the separation distance between adjacent nano-strips. The 2D charge density is modulated by the expression: $N_{2D} = N_{1D}/d$

d (nm)	N_{2D} (cm^{-2})	E_F (eV)
10	1×10^{13}	0.58
20	5×10^{12}	0.41
50	2×10^{12}	0.26
100	1×10^{12}	0.19

Hence, Table 3 provides crucial insights into the relationship between separation distance, charge density, and the associated Fermi level shift in GNSs. Notably, when the separation distance between contiguous nano-strips is merely 10 nm, a couple of noteworthy observations arise:

- First, this configuration yields a substantially high charge density. More intriguingly, it triggers a significant Fermi level shift, measuring 0.58 eV.
- This shift has the potential to introduce an unintended doping effect, which could be problematic, particularly for a 100 nm wide nano-strip characterized by a relatively small bandgap, measuring just a few meV, approximately 46 meV.

In light of these considerations, we have made a strategic choice in our study. We have opted to focus on a charge density of 1×10^{12} cm^{-2}, a value that is widely accepted and routinely employed in modeling graphene and its derivatives [19]. Under these conditions, the Fermi level shift is notably reduced to 0.19 eV, a more manageable and controlled value. Consequently, a separation distance of 100 nm proves to be sufficiently effective for our purposes. By selecting these specific parameters, we strike a balance that minimizes unintended doping effects while allowing the exploration of the desired plasmonic behaviors in GNSs. This careful consideration of separation distance and charge density not only optimizes our experimental setup but also provides a valuable framework for future research involving graphene and related materials, ensuring the reliability and reproducibility of our findings.

Moving forward, Figure 11 provides a comprehensive visualization of the plasmon frequency-momentum dispersion in a 100 nm wide nano-strip, meticulously charting its behavior concerning the reciprocal wave vector. As anticipated, in line with the inherent characteristics of 2D materials, the plasmon dispersion adheres to a $\sqrt{q}$-like behavior. This pattern can be readily explained by the fundamental nature of Equation 1, which governs the plasmonic properties of such systems. What makes this observation particularly intriguing is the profound impact of the separation distance between adjacent nano-strips. As elucidated in Table 3, even a seemingly slight change in this distance, for example, from 10 to 100 nm, significantly influences the plasmon frequency. Specifically, as the separation distance increases, the plasmon frequency undergoes a discernible reduction. This phenomenon can be attributed to a fundamental relationship—namely, that the plasmon frequency is directly proportional to the square root of the 2D charge density, expressed as $\omega_p \sim \sqrt{N_{2D}}$.

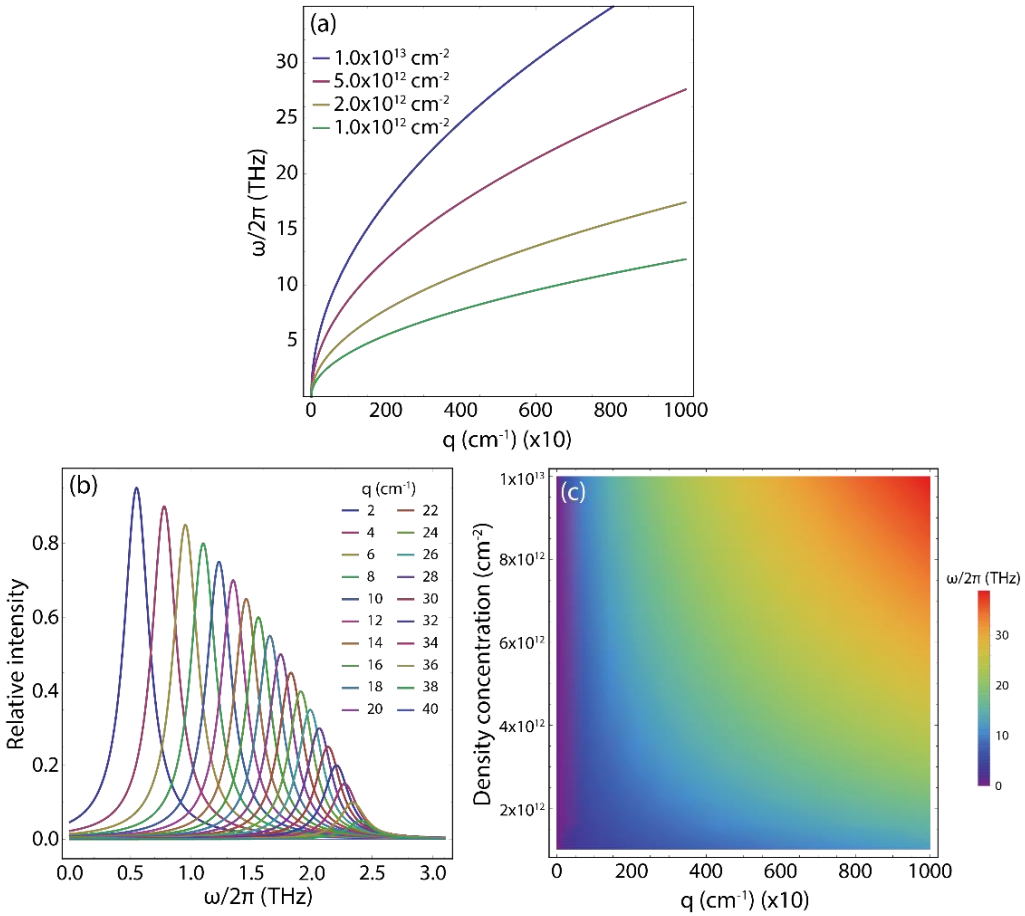

Figure 11. (a) Plasmon frequency-momentum dispersion as a function of the wave vector (q, cm^{-1}), considering different values of charge density (N_{2D}, cm^{-2}) modulated by increasing the separation distance (d, nm) between adjacent nano-strips (Table 3). (b) Maximum of the plasmon peak for selected values of the wave vector. (c) Density plot of plasmon frequency-momentum dispersion as a function of density concentration and wave vector. The analyzed system corresponds to a 100 nm wide nano-strip ($m^* = 3.25 \times 10^{-3} m_0$, $\theta = 0°$, $\nu = 0$).

In essence, this means that as the separation distance between nano-strips widens, the charge density in the system decreases, leading to a corresponding decrease in the plasmon frequency. This relationship underscores the pivotal role played by inter-strip spacing in modulating the plasmonic behavior of graphene nanostructures. It offers valuable insight into how to control and fine-tune plasmon frequencies in these systems, a capability that has far-reaching implications for the design and optimization of plasmonic devices and applications.

Conversely, Figure 11-b provides a detailed depiction of the dispersion of the maximum of the plasmon peak in a 100 nm wide nano-strip. Here, we maintain a charge density of 1×10^{12} cm^{-2}. This analysis is conducted across a spectrum of selected momentum (q) values, encompassing a frequency range spanning from 0.1 to 3 THz. This particular frequency range is chosen because it corresponds to the regime where some of the most pertinent graphene-based plasmonic applications are anticipated to operate. The applications in this range encompass a diverse array of technologies, from THz imaging and spectroscopy to telecommunications and sensing devices.

To accentuate the profound impact of 2D charge density, Figure 11-c provides a comprehensive exploration of its influence, ranging from 1×10^{12} cm^{-2} with a separation distance of 100 nm to 1×10^{13} cm^{-2} with a separation distance of 10 nm. This detailed analysis brings to light two essential observations:

- Forbidden Plasmon Regions: The first striking observation is the emergence of forbidden regions for plasmons, primarily concentrated around values of the reciprocal wave vector (q) close to zero. This forbidden region is visually represented as the distinctive purple region in Figure 11-c. Within this range of wave vectors, plasmonic responses are effectively quenched or suppressed, illustrating a unique quirk in the plasmonic behavior of GNSs.
- Enhanced Spectral Weight: The second noteworthy insight lies in the enhancement of spectral weight with increasing charge density and momentum. As charge density steadily rises, and momentum becomes more substantial, the plasmonic response intensifies significantly. This phenomenon is visually highlighted by the expanding red region in Figure 11-c. At elevated charge densities, particularly around the order of 1×10^{13} cm^{-2}, a distinct plasmon response becomes detectable, extending up to approximately 40 THz. This heightened spectral weight signifies a more pronounced and impactful plasmonic behavior, especially in the higher frequency regime.

These two key observations collectively underscore the intricate interplay between 2D charge density and momentum in governing plasmonic properties in GNSs. The existence of forbidden regions for plasmons near zero wave vector values highlights the constraints within which plasmons operate. Simultaneously, the amplification of the spectral weight with increasing charge density illuminates the potential for precise control over plasmonic responses by manipulating these parameters.

3-5- THz Plasmonics in Exfoliated GNSs

To showcase the outstanding versatility of the semi-analytical model, we draw upon a substantial body of experimental evidence derived from our prior investigations into the exfoliation of graphite [42-45]. These earlier endeavors yielded materials characterized by high concentrations of few-layer graphene and GNSs, thus providing an ideal foundation for the present study. Our primary emphasis in this examination centers on the properties and behaviors of exfoliated GNSs, given that they conform to the specific conditions essential for rigorous analysis using Equation (1). A detailed exposition of the synthesis process and the comprehensive suite of characterization techniques employed can be found in the respective references. It is important to underscore that the synthesis and characterization of these materials, particularly the few-layer graphene and GNSs, constitute a critical backdrop to the current investigation. Leveraging our prior research findings not only enables us to explore the predictive capabilities of the semi-analytical model but also offers a tangible connection to real-world materials.

With this in mind, in Figure 12-a, we provide a comprehensive depiction of the morphology, as ascertained through scanning electron microscopy (SEM). SEM images reveal a distinctive assembly, comprising a mixture of few-layer flakes combined with numerous GNSs. The dimensional characterization of these nanostructures unveils widths spanning the range of 95 to 200 nm, with an average width approximating 135 nm. Notably, this average width represents a remarkable deviation from the findings reported by Yang and Murali [21], who documented widths approximately one-third narrower than our observed strip width values. This substantial width holds significant implications for our study, particularly in the context of utilizing the semi-analytical model for the investigation of these types of nano-strips. Our results suggest that edge effects, which might have played a predominant role in narrower strips, can be significantly mitigated due to the relatively larger dimensions we have observed.

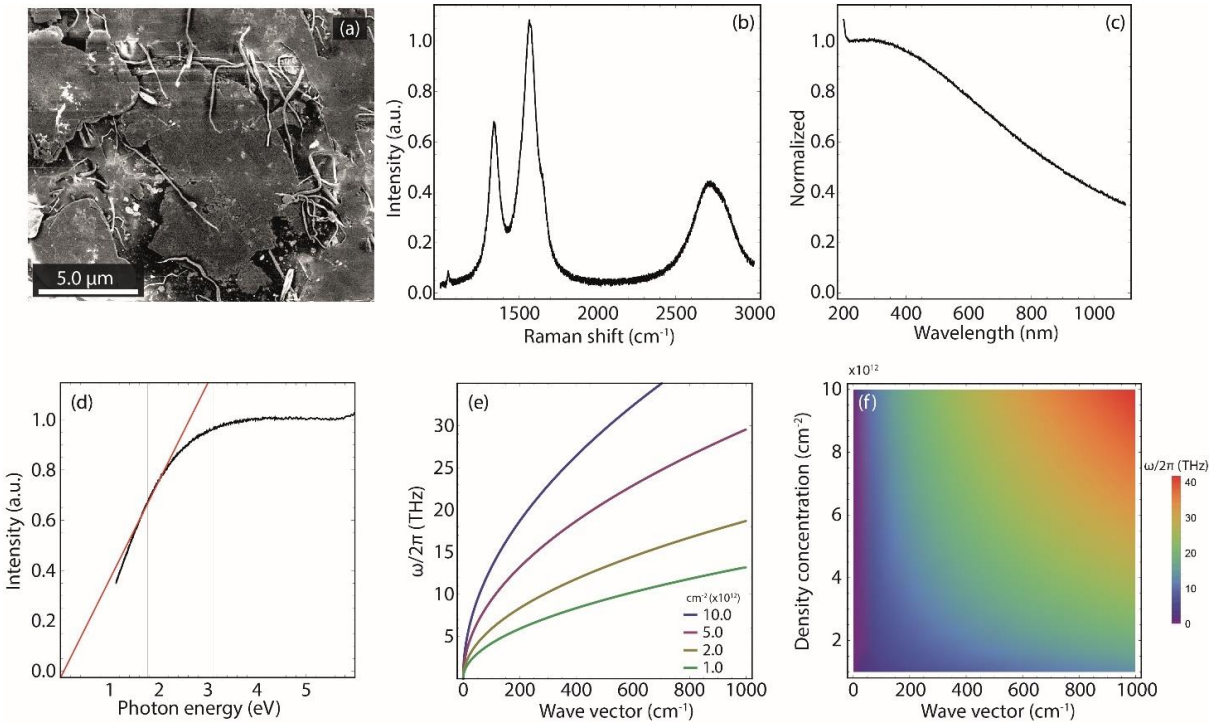

Figure 12. Liquid-phase exfoliated graphene dispersion: (a) SEM morphology, (b) Raman spectrum, (c) Absorbance spectrum, (d) Tauc plot, (e) Plasmon frequency dispersion as a function of the momentum, and (f) Density plot of plasmon frequency-momentum dispersion as a function of density concentration and wave vector.

It is imperative to emphasize that the exfoliated nano-strips under investigation exhibit noticeable bending phenomena across various regions, a phenomenon indicative of the presence of defects. These defects are highly likely to have been introduced during the exfoliation process, thereby warranting meticulous attention during the analysis of these nano-strips. This observation holds paramount significance as it sheds light on the potential impact of structural imperfections on the properties and behaviors of these nanostructures. To substantiate the presence and characterization of these defects, Raman spectroscopy was employed (Figure 12-b). The Raman spectra provide unequivocal evidence of defect-induced perturbations within the nano-strips, as signified by the heightened intensity and prominence of the D and D' peaks, respectively. These pronounced defect-related peaks, when considered in conjunction with the observed reduction in graphene width [46], prompt intriguing possibilities, including the potential for a discernible bandgap. Furthermore, the concurrent presence of the G peak and the 2D peak in the Raman spectrum is a hallmark characteristic typically associated with graphene-derived materials. This spectral signature serves as a corroborative affirmation of the graphene-related nature of the obtained nano-strips

In our pursuit of a comprehensive understanding of the electronic transitions inherent to GNSs, we executed an examination via the collection and subsequent averaging of multiple UV-visible spectra [42] derived from their dispersions. This approach aimed to provide a more representative insight into the electronic behavior of these nanostructures. Hence, the resultant UV-visible absorbance spectrum, as illustrated in Figure 12-c, reveals a conspicuous and broad peak centered at approximately 273 nm. This pronounced absorption peak can be attributed to the $\pi - \pi^*$ transitions of carbon-carbon bonds within the GNSs [45]. The presence of this peak signifies the involvement of electronic transitions characteristic of sp^2 hybridized carbon structures, which aligns with the anticipated behavior of graphene-derived materials. Remarkably, our absorbance spectral analysis did not unveil any additional distinctive features within the visible spectrum range. This observation reinforces the intrinsic electronic stability of the GNSs within the explored wavelength range and suggests that no discernible electronic transitions occur within the visible spectrum region.

Having obtained the absorbance spectrum, we employed the Tauc approach [47], a reliable method for estimating bandgap values in semiconductor materials, to deduce the average bandgap of GNSs, as illustrated in Figure 12-d. Our analysis unveiled a bandgap value of approximately 29 meV for the obtained GNSs. This bandgap magnitude arises from an interplay of several critical factors, notably including the presence of edge and basal defects, as well as the previously discussed reduced width of the GNSs.

These two paramount parameters, namely the width ($w = 135$ nm) and bandgap ($\Delta \approx 30$ meV) serve as critical inputs in Equations (2) and (3). Through these equations, we were able to compute the corresponding effective electron mass, yielding a value of $m^* = 2.83 \times 10^{-3} m_0$. Additionally, we determined the charge-carrier velocity ($v_F = 0.95 \times 10^6$ m s^{-1}) based on these parameters. These precise values of effective mass and charge-carrier velocity are of notable interest as they closely resemble those associated with the 100-nm-wide nano-strip, which has been a focal point of our comprehensive study in the previous subsection.

The acquisition of this effective mass value not only informs our understanding of the electronic properties of the GNSs but also serves as an essential input in Equation 1, which, in turn, enables us to derive the plasmonic properties of the GNSs as a function of the parameters expounded upon in the preceding sections. It is particularly noteworthy that the similarity in effective mass and charge-carrier velocity between the GNSs and the 100 nm wide nano-strip analyzed in this study underscores the robustness and applicability of our findings to a broader range of nanostructures within the same size regime.

Building upon the analytical framework employed in the preceding subsection, we embark on a parallel investigation that yields valuable insights into the behavior of plasmon frequencies. As we delve into this analysis, a pattern emerges an increase in the dispersion of plasmon frequencies. This phenomenon is depicted in Figure 12-e, where we witness a pronounced increase in the propagation of plasmonic responses. Crucially, this upswing in plasmon frequency dispersion is intrinsically linked to the augmentation of 2D charge density. As the charge density within the system steadily rises, the plasmonic behavior responds in kind, giving rise to an important increase in plasmon frequencies. The upper limit of this frequency range extends nearly to the remarkable threshold of 43 THz, delineated by the striking red region showcased in Figure 12-f.

However, as the journey through this intricate realm of plasmonics unfolds, we arrive at a crossroads. The decision of whether to embark on a deeper exploration of these findings, unraveling the complexities of this and other systems such as germanene nano-strips [48], rests entirely in the hands of the reader.

4- Conclusions

In summary, our study leveraged a semi-analytical model hinged upon the charge-carrier velocity of graphene as its primary input parameter. Determining this crucial parameter involved a multi-step process. Initially, we employed DFT calculations within the LDA method (DFT-LDA), which yielded a charge-carrier velocity estimate of $v_F = 0.829 \times 10^6$ m s^{-1}. Subsequently, we refined this result using the more sophisticated GW approximation, leading to an updated velocity value of $v_F = 1.118 \times 10^6$ m s^{-1}. Importantly, our thorough analysis culminated in a charge-carrier velocity that closely mirrors experimental measurements, aligning at $v_F = 1.100 \times 10^6$ m s^{-1}. This alignment underscores the precision and reliability of our proposed modeling approach. With our semi-analytical model established and grounded in the verified charge-carrier velocity of graphene, we performed an extensive exploration of the electronic properties and THz plasmon responses exhibited by GNSs. This comprehensive investigation spanned a diverse range of parameters and variables, offering a holistic and in-depth understanding of the intricate behavior and distinctive characteristics inherent to these nano-strips.

From an electronic property perspective, our findings offer a compelling indication of the behavior of GNSs spanning a width spectrum from 100 nm to 500 nm. Within this range, a striking commonality emerges: these nano-strips exhibit bandgap values that reside in the realm of a few meV. To be more precise, consider a nano-strip with a width of 100 nm, which displays a bandgap of approximately 46 meV. In contrast, a wider nano-strip, measuring 500 nm in width, registers a bandgap that dips below 10 meV. The significance of these observations extends beyond mere numerical values. What truly underscores the power of the semi-analytical model is its capacity to replicate the DOS observed in an experimental counterpart, a nano-strip measuring 2.7 nm width [39]. At this ultranarrow scale in width, the electronic properties of the system are profoundly influenced by edge-chiral effects, rendering the behavior inherently intricate and challenging to model accurately. Remarkably, the semi-analytical model rises to the occasion, successfully mirroring the DOS of this extremely narrow nano-strip. This achievement served as a resounding validation of both the efficacy and precision of our modeling approach. It not only reaffirms the utility of our model for the analysis and prediction of GNS behavior but also highlights its unique capability to capture the intricacies of exceedingly narrow nanostructures, where edge effects wield a substantial influence.

Conversely, from a plasmonic perspective, the semi-analytical model has achieved an impressive feat: it has adeptly reproduced the plasmonic behavior observed in a 4-μm microstrip, as reported experimentally [39]. This remarkable alignment between our modeling approach and experimental observations served as a resounding testament to its accuracy and predictive capabilities in the realm of plasmonic responses. By successfully reflecting the complex interplay of electromagnetic fields and charge carriers within the 4 μm microstrip, our approach affirms its efficacy in capturing the plasmonic behavior.

Building upon this validation, our study has embarked on an extensive exploration, taking us across a spectrum of GNSs ranging from 100 to 500 nm in width. Within this broad span of nano-strips, we have conducted a meticulous examination of the influence of charge density on their plasmonic response. This investigation has unveiled the profound and nuanced effects that variations in 2D charge density can have on the plasmonic characteristics of GNSs, shedding light on the rich possibilities for tailored plasmonic behavior and future plasmonic devices.

Furthermore, our research has illuminated the adaptability of the semi-analytical model. Beyond its theoretical prowess, this adaptability extends to the realm of practical materials, exemplified by our exploration of exfoliated nano-strips with an average width of 135 nm. In this context, our modeling approach served as a versatile bridge, facilitating the seamless transition from theoretical predictions to the study of real-world materials. This capacity enhances our capacity to comprehend and manipulate plasmonic phenomena in graphene-based nanostructures.

A crucial observation gleaned from our study is the consistent manifestation of a square-root-like plasmon dispersion pattern across all the examined nano-strips. This behavior emerges prominently within the THz frequency regime, approximately around 40 THz, and it showcases a noteworthy feature: the ability to finely tune the corresponding plasmon frequency. Regardless, as the plasmon response is deliberately shifted to higher momentum levels, certain spatial locations within the nano-strips become less conducive to sustaining plasmons ($q \sim 0$). These findings emphasize the significant potential inherent in the manipulation and modulation of plasmonic behavior within GNSs.

Finally, our research has provided a comprehensive insight into the intricate electronic and plasmonic attributes of GNSs. This understanding holds paramount importance in the context of advancing and designing future nanodevices. Subsequent research endeavors aimed at corroborating and expanding upon our findings stand to gain significantly from the knowledge acquired through our present study. In essence, our work lays a solid foundation, serving as a valuable resource and reference point for future investigations in this field.

5- Declarations

5-1- Author Contributions

Conceptualization, T.T., C.V.G., and S.B.; methodology, G.M., E.C., N.B., and C.V.G.; validation, T.T., M.G., and C.V.G.; formal analysis, C.V.G.; resources, T.T.; data curation, T.T.; writing—original draft preparation, C.V.G.; writing—review & editing, C.V.G.; visualization, M.G.; project administration, T.T.; funding acquisition, T.T. All authors have read and agreed to the published version of the manuscript.

5-2- Data Availability Statement

The data presented in this study are available on request from the corresponding author.

5-3- Funding

This work was funded by Universidad Técnica Particular de Loja ("Análisis de las propiedades térmicas del grafeno y zeolita" Grand No.: PROY_INV_QU_2022_362).

5-4- Acknowledgements

T.T., M.G., and C.V.G. wish to thank the Ecuadorian National Department of Sciences and Technology (SENESCYT). This work was partially supported by LNF-INFN: Progetto HPSWFOOD Regione Lazio - CUP I35F20000400005.

5-5- Institutional Review Board Statement

Not applicable.

5-6- Informed Consent Statement

Not applicable.

5-7- Conflicts of Interest

The authors declare that there is no conflict of interest regarding the publication of this manuscript. In addition, the ethical issues, including plagiarism, informed consent, misconduct, data fabrication and/or falsification, double publication and/or submission, and redundancies have been completely observed by the authors.

6- References

[1] Dai, Y., Zhou, Z., Ghosh, A., Mong, R. S. K., Kubo, A., Huang, C. Bin, & Petek, H. (2020). Plasmonic topological quasiparticle on the nanometre and femtosecond scales. Nature, 588(7839), 616–619. doi:10.1038/s41586-020-3030-1.

[2] Boerigter, C., Campana, R., Morabito, M., & Linic, S. (2016). Evidence and implications of direct charge excitation as the dominant mechanism in plasmon-mediated photocatalysis. Nature Communications, 7(1), 10545. doi:10.1038/ncomms10545.

[3] Chen, H., Shao, L., Li, Q., & Wang, J. (2013). Gold nanorods and their plasmonic properties. Chemical Society Reviews, 42(7), 2679–2724. doi:10.1039/c2cs35367a.

[4] Zhang, J., Zhang, L., & Xu, W. (2012). Surface plasmon polaritons: Physics and applications. Journal of Physics D: Applied Physics, 45(11), 113001. doi:10.1088/0022-3727/45/11/113001.

[5] Song, X., Wang, Y., Zhao, F., Li, Q., Ta, H. Q., Rümmeli, M. H., Tully, C. G., Li, Z., Yin, W. J., Yang, L., Lee, K. B., Yang, J., Bozkurt, I., Liu, S., Zhang, W., & Chhowalla, M. (2019). Plasmon-Free Surface-Enhanced Raman Spectroscopy Using Metallic 2D Materials. ACS Nano, 13(7), 8312–8319. doi:10.1021/acsnano.9b03761.

[6] Soldano, C., Mahmood, A., & Dujardin, E. (2010). Production, properties and potential of graphene. Carbon, 48(8), 2127–2150. doi:10.1016/j.carbon.2010.01.058.

[7] Grigorenko, A. N., Polini, M., & Novoselov, K. S. (2012). Graphene plasmonics. Nature Photonics, 6(11), 749–758. doi:10.1038/nphoton.2012.262.

[8] García de Abajo, F. J. (2014). Graphene Plasmonics: Challenges and Opportunities. ACS Photonics, 1(3), 135–152. doi:10.1021/ph400147y.

[9] Ni, G. X., McLeod, A. S., Sun, Z., Wang, L., Xiong, L., Post, K. W., Sunku, S. S., Jiang, B.-Y., Hone, J., Dean, C. R., Fogler, M. M., & Basov, D. N. (2018). Fundamental limits to graphene plasmonics. Nature, 557(7706), 530–533. doi:10.1038/s41586-018-0136-9.

[10] Karimi, F., & Knezevic, I. (2017). Plasmons in graphene nanoribbons. Physical Review B, 96(12), 125417. doi:10.1103/PhysRevB.96.125417.

[11] Dutta, S., & Pati, S. K. (2010). Novel properties of graphene nanoribbons: A review. Journal of Materials Chemistry, 20(38), 8207–8223. doi:10.1039/c0jm00261e.

[12] Tian, C., Miao, W., Zhao, L., & Wang, J. (2023). Graphene nanoribbons: Current status and challenges as quasi-one-dimensional nanomaterials. Reviews in Physics, 10, 100082. doi:10.1016/j.revip.2023.100082.

[13] Zhuang, H., Kong, F., Li, K., & Sheng, S. (2015). Plasmonic bandpass filter based on graphene nanoribbon. Applied Optics, 54(10), 2558. doi:10.1364/ao.54.002558.

[14] Silveiro, I., Ortega, J. M. P., & Abajo, F. J. G. De. (2015). Plasmon wave function of graphene nanoribbons. New Journal of Physics, 17(8), 83013. doi:10.1088/1367-2630/17/8/083013.

[15] Fei, Z., Goldflam, M. D., Wu, J. S., Dai, S., Wagner, M., McLeod, A. S., Liu, M. K., Post, K. W., Zhu, S., Janssen, G. C. A. M., Fogler, M. M., & Basov, D. N. (2015). Edge and Surface Plasmons in Graphene Nanoribbons. Nano Letters, 15(12), 8271–8276. doi:10.1021/acs.nanolett.5b03834.

[16] Gomez, C. V., Pisarra, M., Gravina, M., & Sindona, A. (2017). Tunable plasmons in regular planar arrays of graphene nanoribbons with armchair and zigzag-shaped edges. Beilstein Journal of Nanotechnology, 8(1), 172–182. doi:10.3762/bjnano.8.18.

[17] Andersen, D. R., & Raza, H. (2012). Plasmon dispersion in semimetallic armchair graphene nanoribbons. Physical Review B, 85(7). doi:10.1103/physrevb.85.075425.

[18] Xia, S., Zhai, X., Wang, L., Li, H., Huang, Z., & Lin, Q. (2015). Dynamically tuning the optical coupling of surface plasmons in coplanar graphene nanoribbons. Optics Communications, 352, 110–115. doi:10.1016/j.optcom.2015.05.002.

[19] Popov, V. V., Bagaeva, T. Y., Otsuji, T., & Ryzhii, V. (2010). Oblique terahertz plasmons in graphene nanoribbon arrays. Physical Review B - Condensed Matter and Materials Physics, 81(7), 73404. doi:10.1103/PhysRevB.81.073404.

[20] Tene, T., Guevara, M., Viteri, E., Maldonado, A., Pisarra, M., Sindona, A., Gomez, C. V., & Bellucci, S. (2022). Calibration of Fermi Velocity to Explore the Plasmonic Character of Graphene Nanoribbon Arrays by a Semi-Analytical Model. Nanomaterials, 12(12). doi:10.3390/nano12122028.

[21] Yang, Y., & Murali, R. (2010). Impact of size effect on graphene nanoribbon transport. IEEE Electron Device Letters, 31(3), 237–239. doi:10.1109/LED.2009.2039915.

[22] Tene, T., Guevara, M., Cevallos, Y., Sáez Paguay, M. Á., Bellucci, S., & Vacacela Gomez, C. (2023). THz Surface Plasmons in Wide and Freestanding Graphene Nanoribbon Arrays. Coatings, 13(1), 28. doi:10.3390/coatings13010028.

[23] Tene, T., Guevara, M., Svozilík, J., Coello-Fiallos, D., Briceño, J., & Vacacela Gomez, C. (2022). Proving Surface Plasmons in Graphene Nanoribbons Organized as 2D Periodic Arrays and Potential Applications in Biosensors. Chemosensors, 10(12), 514. doi:10.3390/chemosensors10120514.

[24] Tene, T., Guevara, M., Borja, M., Mendoza Salazar, M. J., Palacios Robalino, M. de L., Vacacela Gomez, C., & Bellucci, S. (2023). Modeling semiconducting silicene nanostrips: electronics and THz plasmons. Frontiers in Physics, 11, 1198214. doi:10.3389/fphy.2023.1198214.

[25] Ratnawati, R., Wulandari, R., Kumoro, A. C., & Hadiyanto, H. (2022). Response surface methodology for formulating PVA/starch/lignin biodegradable plastic. Emerging Science Journal, 6(2), 238-255. doi:10.28991/ESJ-2022-06-02-03.

[26] Sindona, A., Vacacela Gomez, C., & Pisarra, M. (2022). Dielectric screening versus geometry deformation in two-dimensional allotropes of silicon and germanium. Scientific Reports, 12(1), 15107. doi:10.1038/s41598-022-19260-y.

[27] Gori-Giorgi, P., Seidl, M., & Vignale, G. (2009). Density-Functional Theory for Strongly Interacting Electrons. Physical Review Letters, 103(16). doi:10.1103/physrevlett.103.166402.

[28] Troullier, N., & Martins, J. (1990). A straightforward method for generating soft transferable pseudopotentials. Solid State Communications, 74(7), 613–616. doi:10.1016/0038-1098(90)90686-6.

[29] Sindona, A., Pisarra, M., Bellucci, S., Tene, T., Guevara, M., & Vacacela Gomez, C. (2019). Plasmon oscillations in two-dimensional arrays of ultranarrow graphene nanoribbons. Physical Review B, 100(23), 235422. doi:10.1103/PhysRevB.100.235422.

[30] Wisesa, P., McGill, K. A., & Mueller, T. (2016). Efficient generation of generalized Monkhorst-Pack grids through the use of informatics. Physical Review B, 93(15), 155109. doi:10.1103/PhysRevB.93.155109.

[31] Aryasetiawan, F., & Gunnarsson, O. (1998). The GW method. Reports on Progress in Physics, 61(3), 237–312. doi:10.1088/0034-4885/61/3/002.

[32] Hagen, G., Vaagen, J. S., & Hjorth-Jensen, M. (2004). The contour deformation method in momentum space, applied to subatomic physics. Journal of Physics A: Mathematical and General, 37(38), 8991–9021. doi:10.1088/0305-4470/37/38/006.

[33] Zhang, Y., Tan, Y. W., Stormer, H. L., & Kim, P. (2005). Experimental observation of the quantum Hall effect and Berry's phase in graphene. Nature, 438(7065), 201–204. doi:10.1038/nature04235.

[34] Jacak, W. A. (2015). Lorentz friction for surface plasmons in metallic nanospheres. Journal of Physical Chemistry C, 119(12), 6749–6759. doi:10.1021/jp511560g.

[35] Egerton, R. F. (2009). Electron energy-loss spectroscopy in the TEM. Reports on Progress in Physics, 72(1), 16502. doi:10.1088/0034-4885/72/1/016502.

[36] Han, M. Y., Özyilmaz, B., Zhang, Y., & Kim, P. (2007). Energy Band-Gap Engineering of Graphene Nanoribbons. Physical Review Letters, 98(20). doi:10.1103/physrevlett.98.206805.

[37] Yang, L., Park, C.-H., Son, Y.-W., Cohen, M. L., & Louie, S. G. (2007). Quasiparticle Energies and Band Gaps in Graphene Nanoribbons. Physical Review Letters, 99(18). doi:10.1103/physrevlett.99.186801.

[38] Kiraly, B., Mannix, A. J., Jacobberger, R. M., Fisher, B. L., Arnold, M. S., Hersam, M. C., & Guisinger, N. P. (2016). Sub-5 nm, globally aligned graphene nanoribbons on Ge(001). Applied Physics Letters, 108(21). doi:10.1063/1.4950959.

[39] Ju, L., Geng, B., Horng, J., Girit, C., Martin, M., Hao, Z., Bechtel, H. A., Liang, X., Zettl, A., Shen, Y. R., & Wang, F. (2011). Graphene plasmonics for tunable terahertz metamaterials. Nature Nanotechnology, 6(10), 630–634. doi:10.1038/nnano.2011.146.

[40] Tao, C., Jiao, L., Yazyev, O. V., Chen, Y. C., Feng, J., Zhang, X., Capaz, R. B., Tour, J. M., Zettl, A., Louie, S. G., Dai, H., & Crommie, M. F. (2011). Spatially resolving edge states of chiral graphene nanoribbons. Nature Physics, 7(8), 616–620. doi:10.1038/nphys1991.

[41] Ryu, S., Maultzsch, J., Han, M. Y., Kim, P., & Brus, L. E. (2011). Raman spectroscopy of lithographically patterned graphene nanoribbons. ACS Nano, 5(5), 4123–4130. doi:10.1021/nn200799y.

[42] Vacacela Gomez, C., Guevara, M., Tene, T., Villamagua, L., Usca, G. T., Maldonado, F., Tapia, C., Cataldo, A., Bellucci, S., & Caputi, L. S. (2021). The liquid exfoliation of graphene in polar solvents. Applied Surface Science, 546, 149046. doi:10.1016/j.apsusc.2021.149046.

[43] Gomez, C. V., Tene, T., Guevara, M., Usca, G. T., Colcha, D., Brito, H., Molina, R., Bellucci, S., & Tavolaro, A. (2019). Preparation of few-layer graphene dispersions from hydrothermally expanded graphite. Applied Sciences (Switzerland), 9(12), 2539. doi:10.3390/app9122539.

[44] Usca, G. T., Gomez, C. V., Guevara, M., Tene, T., Hernandez, J., Molina, R., Tavolaro, A., Miriello, D., & Caputi, L. S. (2019). Zeolite-assisted shear exfoliation of graphite into few-layer graphene. Crystals, 9(8), 377. doi:10.3390/cryst9080377.

[45] Cayambe, M., Zambrano, C., Tene, T., Guevara, M., Usca, G. T., Brito, H., Molina, R., Coello-Fiallos, D., Caputi, L. S., & Gomez, C. V. (2019). Dispersion of graphene in ethanol by sonication. Materials Today: Proceedings, 37, 4027–4030. doi:10.1016/j.matpr.2020.06.441.

[46] Villamagua, L., Carini, M., Stashans, A., & Gomez, C. V. (2016). Band gap engineering of graphene through quantum confinement and edge distortions. Ricerche Di Matematica, 65(2), 579–584. doi:10.1007/s11587-016-0278-8.

[47] Feng, Y., Lin, S., Huang, S., Shrestha, S., & Conibeer, G. (2015). Can Tauc plot extrapolation be used for direct-band-gap semiconductor nanocrystals? Journal of Applied Physics, 117(12), 125701. doi:10.1063/1.4916090.

[48] Tene, T., Guevara, M., Tubon-Usca, G., Cáceres, O. V., Moreano, G., Gomez, C. V., & Bellucci, S. (2023). THz plasmonics and electronics in germanene nanostrips. Journal of Semiconductors, 44(10), 102001-1.